Hindawi Publishing Corporation
Advances in OptoElectronics
Volume 2013, Article ID 840931, 12 pages
http://dx.doi.org/10.1155/2013/840931

Research Article

The Effect of Electron versus Hole Photocurrent on Optoelectric Properties of p^+-p-n-n^+ Wz-GaN Reach-Through Avalanche Photodiodes

Moumita Ghosh,[1] Mangolika Mondal,[1] and Aritra Acharyya[2]

[1] *Supreme Knowledge Foundation Group of Institutions, Sir J. C. Bose School of Engineering, 1, Khan Road, Mankundu, Hooghly, West Bengal 712139, India*
[2] *Institute of Radio Physics and Electronics, University of Calcutta, 92, APC Road, Kolkata, West Bengal 700009, India*

Correspondence should be addressed to Aritra Acharyya; ari_besu@yahoo.co.in

Received 23 November 2012; Accepted 15 January 2013

Academic Editor: Xian Cao

The authors have made an attempt to investigate the effect of electron versus hole photocurrent on the optoelectric properties of p^+-p-n-n^+ structured Wurtzite-GaN (Wz-GaN) reach-through avalanche photodiodes (RAPDs). The photo responsivity and optical gain of the devices are obtained within the wavelength range of 300 to 450 nm using a novel modeling and simulation technique developed by the authors. Two optical illumination configurations of the device such as Top Mounted (TM) and Flip Chip (FC) are considered for the present study to investigate the optoelectric performance of the device separately due to electron dominated and hole dominated photocurrents, respectively, in the visible-blind ultraviolet (UV) spectrum. The results show that the peak unity gain responsivity and corresponding optical gain of the device are 555.78 mA W^{-1} and 9.4144×10^3, respectively, due to hole dominated photocurrent (i.e., in FC structure); while those are 480.56 mA W^{-1} and 7.8800×10^3, respectively, due to electron dominated photocurrent (i.e., in TM structure) at the wavelength of 365 nm and for applied reverse bias of 85 V. Thus, better optoelectric performance of Wz-GaN RAPDs can be achieved when the photocurrent is made hole dominated by allowing the UV light to be shined on the n^+-layer instead of p^+-layer of the device.

1. Introduction

Ultraviolet detectors are of a great interest to a wide range of industrial, defense, scientific, commercial, environmental, and even biological applications. Most of these applications inherently require high sensitivity, low noise, and visible-blind detection. Photomultiplier tubes (PMTs) may be used as UV detectors due to their large internal gain (~10^6) which ensures high detectivity in UV range. However, the drawbacks of PMTs are as follows: they are bulky, and they require large bias voltage (~1000 V) for operation [1]. Thus, the semiconductor-based alternatives such as avalanche photodiodes (APDs) are preferred over PMTs due to their small size, high gain and also they require much lower voltage for biasing. APDs working in ultraviolet (UV) range are in immense interest of researchers nowadays for numerous applications, including bioaerosol detection, UV imaging, harsh environment gamma sensing [2] and long-range flame detection in the solar-blind window. Conventional Si APDs generally have limited deep-UV quantum efficiency and appreciable visible response [3, 4]. Thus, additional filtering is essential for them to operate in deep-UV range. Further, very low quantum efficiency of Si APDs at these range make them inefficient. APDs based on wide bandgap semiconductors such as GaN [5] and SiC [6] offer natural visible blindness, harsh environment capability and low noise performance. However, SiC-based APDs require additional filtering to operate in the deep-UV range which further limits their sensitivity and applicability. GaN-based APDs are the most promising semiconductor-based photodetectors to operate in deep-UV range which offer the potential self-filtering solar blindness with sharp responsivity cutoff [7]. GaN (bandgap $E_g = 3.4$ eV) grown on sapphire substrate has shown high performance visible-blind UV detection [8]. Since early

2000, several researchers have fabricated and characterized the GaN- or GaN/AlGaN-based APDs (homojunction or heterojunction) and explored the potentiality of GaN as base material of APDs for deep-UV sensing [9–19].

But so far, as authors' knowledge is concerned, no experimental or theoretical verification is available in the published literatures till the date investigating the effect of electron dominated and hole dominated photocurrents separately on the optoelectric performance of GaN APDs in UV range. In the present paper, the authors have carried out simulation experiment on p^+-p-n-n^+ structured Wz-GaN reach-through avalanche photodiodes (RAPDs) for two types of device orientations used to illuminate the UV light on the device to investigate the photosensitivity and optical gain of the device by using a novel modeling and simulation technique developed by the authors [20, 21]. Band-to-band tunneling and trap-assisted tunneling mechanisms are incorporated into the simulation method used in the present study; those were not considered in the previous papers by the authors [20, 21]. Simulation is carried out to investigate the electric and optoelectric performance of UV RAPDs based on Wz-GaN for the following two illumination configurations: (a) light is incident on back p^+-layer of the p^+-p-n-n^+ structured device (i.e., TM structure) and (b) light is incident on top n^+-layer of the device (i.e., FC structure). In the first configuration, (a) the electron component of photocurrent dominates over the hole component of the same, while in the second one, (b) the hole component of photocurrent dominates over the electron component. The optoelectronic properties of Wz-GaN RAPDs under both types of optical illumination configurations have been compared in this paper, and the superior configuration is suggested.

2. Material Parameters

The optical gain and responsivity of Wz-GaN RAPDs are sensitive functions of electric field (ξ). The electric field variation of carrier ionization rates in Wz-GaN is given by

$$\alpha_{n,p}(\xi) = A_{n,p} \exp\left[\left(\frac{-B_{n,p}}{\xi}\right)^m\right], \quad (1)$$

where the value of the constant $m = 1$. The values of the ionization coefficients $A_{n,p}$ and $B_{n,p}$ for a wide field range in Wz-GaN are taken from experimental data of Kunihiro et al. [22]. The negative differential mobility in the electron drift velocity versus electric field characteristics (i.e., v_n versus ξ) of group III-IV semiconductors [23, 24] has been taken into account in the computer simulation through the expression

$$v_n(\xi) = \frac{\mu_n \xi + v_{sn}(\xi/\xi_c)^4}{1 + (\xi/\xi_c)^4}, \quad (2)$$

which incorporates a peak in the drift velocity at low field (ξ_c) followed by a velocity saturation (v_{sn}) at high electric field. The hole drift velocity versus field characteristics (i.e., v_p versus ξ) of Wz-GaN is given by

$$v_p(\xi) = v_{sp}\left[1 - \exp\left(\frac{-\mu_p \xi}{v_{sp}}\right)\right]. \quad (3)$$

All other material parameters such as bandgap (E_g), intrinsic carrier concentration (n_i), effective density of states of conduction and valance bands (N_c, N_v), diffusion coefficients (D_n, D_p), mobilities (μ_n, μ_p), and diffusion lengths (L_n, L_p) of charge carriers and permittivity (ε_s) of Wz-GaN are taken from recently published reports [25]. Necessary optical parameters of Wz-GaN such as absorption coefficient ($\alpha(\lambda)$) and reflectance ($R(\lambda)$) for the wavelength range of 300–450 nm at room temperature (i.e., $T = 300$ K) are taken from experimental report [26, 27].

3. Device Structure

A cross-sectional view of Wz-GaN p^+-p-n-n^+ structured RADP is shown in Figures 1(a) and 1(b), respectively, for two different optical illumination configurations as mentioned earlier. In the first case (Figure 1(a)), light is incident on the top p^+-layer so that the photocurrent due to electrons dominate over that of holes (i.e., TM structure), and in the second case (Figure 1(b)), light is incident on the back n^+-layer so that photocurrent due to holes dominates over that of electrons (i.e., FC structure). The doping levels of the p- and n-layers are designed such that both the layers are totally depleted and lead to reach-through structures. Total depletion of p- and n-layers causes significant improvement in the impulse response of RAPDS due to negligible diffusion photocurrent [28] in the active layer of the device. Also, the reach-through structure improves the responsivity of the device and ensures carrier multiplication without excess noise for a specific thickness of multiplication region within the device [28]. Four different Wz-GaN RAPDs are designed with different doping levels of p- and n-active layers to study the effect of the level of doping on the optoelectric characteristics of the device. The thicknesses of different active layers such as epitaxial n- and p-layers (W_n and W_p) and corresponding doping concentrations (N_D and N_A) are given in Table 1. The thicknesses of n^+-substrate layer and p^+-layer (W_{n^+} and W_{p^+}) are taken as 500 nm and 150 nm, respectively, in top illuminated TM structure, and those are taken as 200 nm, and 150 nm in back illuminated FC structure. The doping concentrations of n^+-substrate layer and p^+-layer (N_{n^+} and N_{p^+}) are taken as 5.0×10^{24} m^{-3} which has been achieved in Wz-GaN [29]. The device junction area is taken as $A_j = 200\ \mu\text{m} \times 200\ \mu\text{m}$ and the illumination area of the device is taken as $A = 60\ \mu\text{m} \times 60\ \mu\text{m}$.

4. Simulation Technique

In this section, the simulation technique used to investigate the electrical and optoelectrical characteristics of p^+-p-n-n^+ structured RAPDs is discussed in detail. Using this technique, the simulation can be carried out for two different optical illumination configurations, that is, TM and FC structures as

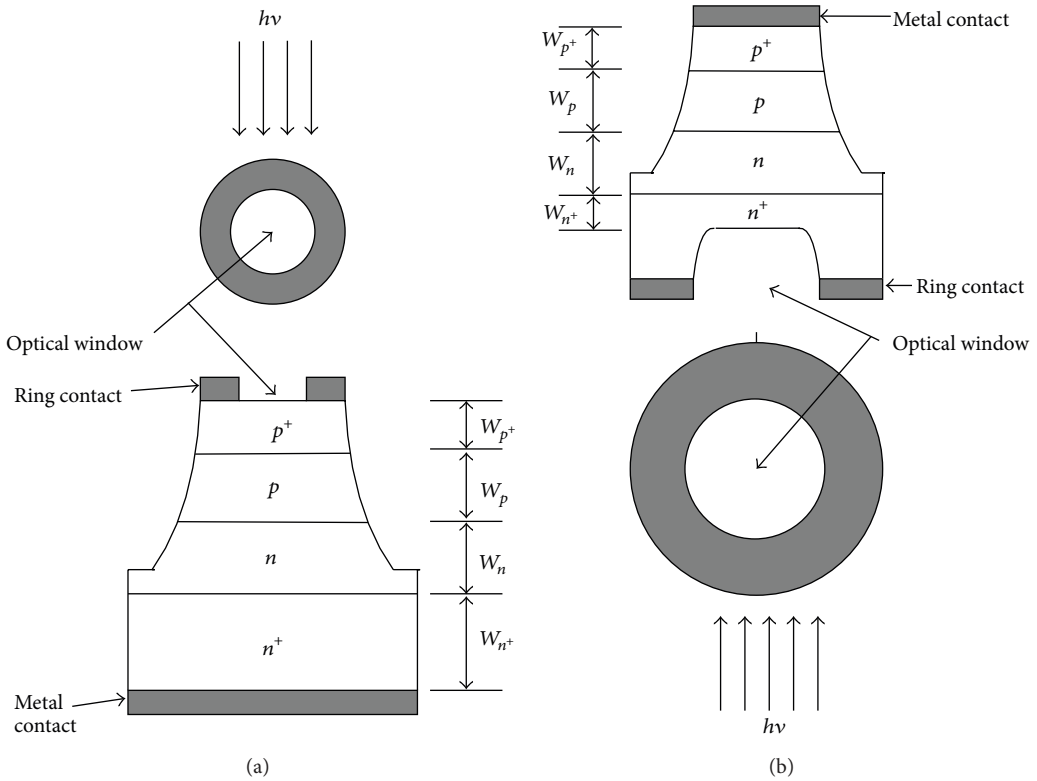

FIGURE 1: Cross-sectional view of the p^+-p-n-n^+ structured Wz-GaN RAPDs for two optical illumination configurations: (a) TM structure (top p^+-layer illuminated) and (b) FC structure (back n^+-layer illuminated).

TABLE 1: Design parameters.

Illumination configuration	Symbol	W_{n^+} (μm)	W_{p^+} (μm)	N_{n^+} ($\times 10^{24}$ m^{-3})	N_{p^+} ($\times 10^{24}$ m^{-3})	W_n (μm)	W_p (μm)	N_D ($\times 10^{23}$ m^{-3})	N_A ($\times 10^{23}$ m^{-3})
TM	RAPD1	0.500	0.150	5.00	5.00	0.440	0.435	2.50	2.60
	RADP2	0.500	0.150	5.00	5.00	0.440	0.435	2.40	2.50
	RAPD3	0.500	0.150	5.00	5.00	0.440	0.435	2.30	2.40
	RADP4	0.500	0.150	5.00	5.00	0.440	0.435	2.20	2.30
FC	RAPD1	0.200	0.150	5.00	5.00	0.440	0.435	2.50	2.60
	RADP2	0.200	0.150	5.00	5.00	0.440	0.435	2.40	2.50
	RAPD3	0.200	0.150	5.00	5.00	0.440	0.435	2.30	2.40
	RADP4	0.200	0.150	5.00	5.00	0.440	0.435	2.20	2.30

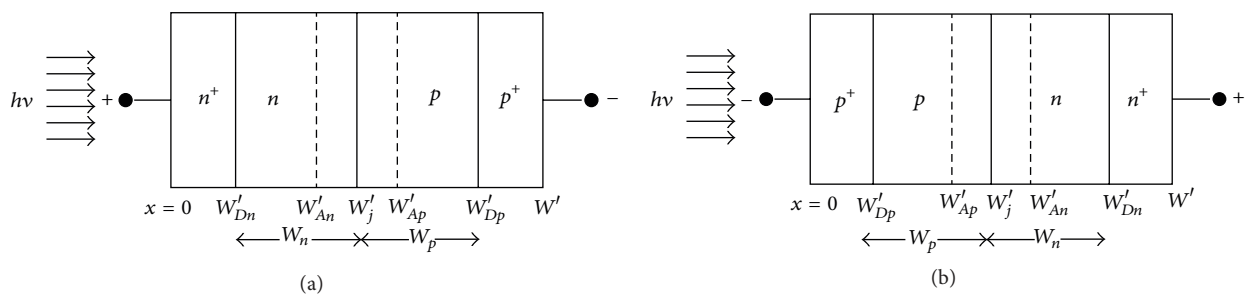

FIGURE 2: One-dimensional model of p^+-p-n-n^+ structured RAPD under two optical illumination configurations, that is, (a) FC structure and (b) TM structure.

mentioned earlier to investigate the electric and optoelectric characteristics of the device. One-dimensional model of reverse biased p^+-p-n-n^+ structure shown in Figure 2 is taken for the simulation of the RAPDs under consideration. The physical phenomena take place in the semiconductor bulk along the symmetry axis of RAPD. Thus, the one-dimensional model of RAPDs considered in this work is justified. The static electric field and normalized current density profiles in the depletion layer of the device are obtained from simultaneous numerical solution of fundamental device equations, that is, Poisson's equation (4), carrier continuity equations in the steady state (5), current density equations (6), and mobile space charge equation (7) subject to appropriate boundary conditions as discussed in the earlier paper by the authors [20, 21]. A double-iterative simulation method is developed by the authors to solve these above-mentioned equations to obtain the DC electric field and normalized current density profiles [20, 21]. The basic device equations are given by

$$\frac{d\xi(x)}{dx} = -\frac{d^2V(x)}{dx^2} = \frac{q}{\varepsilon_s}\left(N_D - N_A + p(x) - n(x)\right), \quad (4)$$

$$\frac{1}{q}\frac{\partial}{\partial x}\left(J_p(x) - J_n(x)\right) = 2G_A(x) + G_{BBTn}(x) + G_{BBTp}(x) + 2G_{TAT}(x), \quad (5)$$

$$J_p(x) = q\left[v_p(x)\left(1 - \frac{D_p}{v_p(x)}\frac{\partial}{\partial x}\right)\right]p(x),$$
$$J_n(x) = q\left[v_n(x)\left(1 + \frac{D_n}{v_n(x)}\frac{\partial}{\partial x}\right)\right]n(x), \quad (6)$$

$$q\frac{\partial\left(p(x) - n(x)\right)}{\partial x} = \left(J_p(x) + J_n(x)\right)\left(\frac{\alpha_n(x)}{v_n(x)} + \frac{\alpha_p(x)}{v_p(x)}\right) - q\left(\alpha_n(x) - \alpha_p(x)\right)\left(p(x) - n(x)\right) + q\left(\frac{G_{BBTn}(x)}{v_n(x)} + \frac{G_{BBTp}(x)}{v_p(x)}\right) + qG_{TAT}(x)\left(\frac{1}{v_n(x)} + \frac{1}{v_p(x)}\right) + \left[\frac{J_p(x)\mu_p}{v_p(x)}\left(\frac{1}{v_{sp}} - \frac{1}{v_p(x)}\right) - \frac{J_n(x)\mu_n}{v_n(x)}\left(\frac{1}{v_{sn}} - \frac{1}{v_n(x)}\right)\right]\left(\frac{\partial\xi(x)}{\partial x}\right), \quad (7)$$

where N_D and N_A are the donor and acceptor concentrations in n- and p-layers, respectively, $p(x)$ and $n(x)$ are, respectively, the electron and hole concentrations at the space point x, $\xi(x)$ and $V(x)$ are, respectively, the electric field and potential at x, $J_n(x)$ and $J_p(x)$ are, respectively the electron and hole components of total current density (J_T), q is the electric charge of an electron (1.6×10^{-19} C), D_n and D_p are the electron and hole diffusion coefficients, and ε_s is the permittivity of the semiconductor material.

The G_A is the avalanche generation rate given by

$$G_A(x) = \alpha_n(x)\, v_n(x)\, n(x) + \alpha_p(x)\, v_p(x)\, p(x), \quad (8)$$

where $\alpha_n(x)$ and $\alpha_p(x)$ are the ionization rates, $v_n(x)$ and $v_p(x)$ are the drift velocities of electrons and holes at the space point x within the depletion layer of the device. Recombination effects are not included in the analysis since the transit time of carriers in the depletion layer of an APD is several orders of magnitude shorter than the recombination time. The band-to-band tunneling generation rate for electrons (G_{BBTn}) obtained from quantum mechanical considerations [30–32] is given by

$$G_{BBTn}(x) = a_T\xi^2(x)\exp\left(-\frac{b_T}{\xi(x)}\right), \quad (9)$$

where the coefficients a_T and b_T are given by

$$a_T = \frac{q^2}{8\pi^3\hbar^2}\left(\frac{2m^*}{E_g}\right)^{1/2},$$
$$b_T = \frac{1}{2q\hbar}\left(\frac{m^*E_g^3}{2}\right)^{1/2}, \quad (10)$$

where m^* is the density of state elective mass of charge carriers, E_g is the bandgap of the semiconductor, $\hbar = h/2\pi$, and $h = 6.625 \times 10^{-34}$ J s is the Planck's constant. The band-to-band tunneling generation rate for holes can be obtained from Figure 3. The phenomenon of band-to-band tunneling is instantaneous, and the band-to-band tunnel generation rate for holes at x is equal to that for electrons at x' that is, $G_{BBTp}(x) = G_{BBTn}(x')$. The band-to-band tunnel generation of an electron at x' is simultaneously associated with the generation of a hole at x, where $(x - x')$ is the spatial separation between the edge of conduction band and valence band at the same energy. If E is the measure of energy from the bottom of the conduction band on the n-side and the vertical difference between x and x' is E_g, x'can be easily obtained from Figure 3 as [33, 34]

$$x = x'\left(1 - \frac{E_g}{E}\right)^{-1/2} \quad \text{for } 0 \le x \le x_j,$$
$$x = W - \left(W - x'\right)\left(1 + \frac{E_g}{E_B - E}\right)^{-1/2} \quad \text{for } x_j \le x \le W. \quad (11)$$

The hole generation rate due to band-to-band tunneling is zero in the region defined by $0 \le x \le x_L$ (Figure 3) as electrons in the valance band find no available states in the conduction band for band-to-band tunneling. Similarly, nonavailability of states in the conduction band for tunneling to take place in the region $x_R \le x \le W$ (Figure 3) makes no contribution of band-to-band tunnel generated electrons in this region.

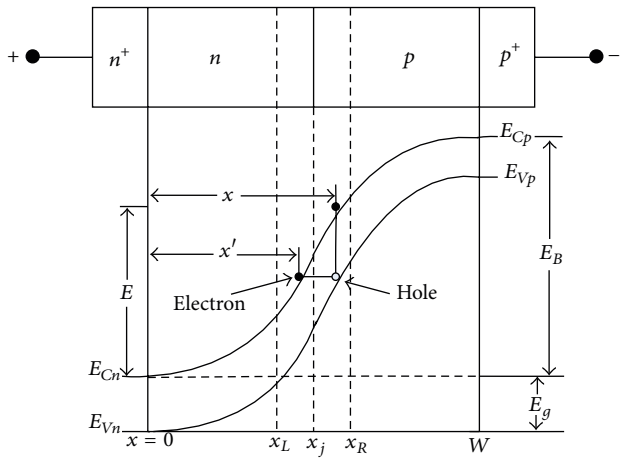

Figure 3: One-dimensional model of a reverse biased ADP and associated energy-band diagram (showing the band-to-band tunneling positions of electrons and holes).

The band-to-band tunneling component of current density can be calculated as

$$J_{BBT} = q \int_{W_{D_n}}^{W_{D_p}} \left[G_{BBTn}(x) + G_{BBTp}(x)\right] dx, \quad \text{in FC structure,}$$
$$J_{BBT} = q \int_{W'_{D_p}}^{W'_{D_n}} \left[G_{BBTn}(x) + G_{BBTp}(x)\right] dx, \quad \text{in TM structure.} \tag{12}$$

The trap-assisted tunneling generation rate ($G_{TAT}(x)$) at the space point x within the depletion layer is given by

$$G_{TAT}(x) = \frac{1}{q}\frac{dJ_{TAT}(x)}{dx}, \tag{13}$$

where $J_{TAT}(x)$ is the trap-assisted tunneling component of current density at the space point x calculated on the basis of simple one-dimensional model [35] that can be written as

$$J_{TAT}(x) = \frac{q^3 m_n^* \xi(x) M_x^2 W N_T}{8\pi\hbar^3 \left(E_g - E_t\right)} \times \exp\left(-\frac{4\sqrt{2m_n^* \left(E_g - E_t\right)^3}}{3q\hbar\xi(x)}\right), \tag{14}$$

where E_t is the energy (eV) corresponding to the trap centers measured from top of the valance band, m_n^* is the effective mass of electrons, N_T is the density of traps occupied by electrons, and M_x is the matrix element associated with the trap potential [35]. Thus, the total current density in unilluminated APD can be written as

$$J_T = J_A + J_{BBT} + J_{TAT}, \tag{15}$$

where J_A is the avalanche component of the current density given by

$$J_A = q \int_{W_{D_n}}^{W_{D_p}} G_A(x)\, dx \quad \text{in FC structure,}$$
$$J_A = q \int_{W'_{D_p}}^{W'_{D_n}} G_A(x)\, dx \quad \text{in TM structure.} \tag{16}$$

Proper boundary conditions of electric field and normalized current density for the simultaneous numerical solution of (4) to (7) are essential. The boundary conditions for the electric field at the depletion layer edges (Figure 2) are given by

$$\xi\left(x = W_{D_n}\right) = 0, \quad \xi\left(x = W_{D_p}\right) = 0, \quad \text{in FC structure,} \tag{17a}$$

$$\xi\left(x = W'_{D_p}\right) = 0, \quad \xi\left(x = W'_{D_n}\right) = 0, \quad \text{in TM structure.} \tag{17b}$$

Similarly, the boundary conditions for normalized current density, $P(x) = [J_p(x) - J_n(x)/J_T]$ at the depletion layer edges (Figure 2) are given by

$$P\left(x = W_{D_n}\right) = \left(\frac{2}{M_p\left(x = W_{D_n}\right)} - 1\right),$$
$$P\left(x = W_{D_p}\right) = \left(1 - \frac{2}{M_n\left(x = W_{D_p}\right)}\right), \tag{18a}$$

in unilluminated FC structure,

$$P\left(x = W'_{D_p}\right) = \left(1 - \frac{2}{M_n\left(x = W'_{D_p}\right)}\right),$$
$$P\left(x = W'_{D_n}\right) = \left(\frac{2}{M_p\left(x = W'_{D_n}\right)} - 1\right), \tag{18b}$$

in unilluminated TM structure,

where $M_n(x)$ and $M_p(x)$ are the position dependent electron and hole multiplication factors [20, 36]. Assuming that the carrier multiplication occurs only within the avalanche region, it can be concluded that the electron multiplication factor at the edge of the depletion layer at n-side is the same as the electron multiplication factor at the edge of the avalanche zone at n-side, that is,

$$M_n\left(x = W_{D_n}\right) = M_n\left(x = W_{A_n}\right),$$
$$M_n\left(x = W'_{D_n}\right) = M_n\left(x = W'_{A_n}\right). \tag{19}$$

Similarly, the hole multiplication factor at the edge of the depletion layer at p-side is the same as hole multiplication factor at the edge of the avalanche zone in p-side, that is,

$$M_p\left(x = W_{D_p}\right) = M_n\left(x = W_{A_p}\right),$$
$$M_p\left(x = W'_{D_p}\right) = M_p\left(x = W'_{A_p}\right). \tag{20}$$

The electron and hole multiplication factors of unilluminated APD at the n- and p-depletion layer edges are given by

$$M_n = \frac{J_T}{J_{ns(\mathrm{Th})}}, \qquad M_p = \frac{J_T}{J_{ps(\mathrm{Th})}}, \tag{21}$$

where $J_{ns(\mathrm{Th})}$ is the total thermally generated reverse saturation current ($J_{(\mathrm{Th})} = J_{ns(\mathrm{Th})} + J_{ps(\mathrm{Th})}$). The expression for thermally generated electron and hole reverse saturation currents are given by

$$J_{ns(\mathrm{Th})} = \left(\frac{qD_n n_i^2}{L_n N_A}\right), \qquad J_{ps(\mathrm{Th})} = \left(\frac{qD_p n_i^2}{L_p N_D}\right). \tag{22}$$

If P_{in} watts of optical power is incident on the device having effective device illumination area of A, then the photon flux density Φ_0 is given by

$$\Phi_0 = P_{in}\frac{(1 - R(\lambda))\,\lambda}{Ahc}. \tag{23}$$

The electron-hole pair (EHP) generation rate ($G_L(x)$) at the space point x of the depletion region due to optical illumination is given by

$$G_L(x) = \Phi_0 \alpha(\lambda) \exp(-\alpha(\lambda)\,x)$$
$$= P_{in}\frac{\alpha(\lambda)\,(1 - R(\lambda))\,\lambda}{Ahc}\exp(-\alpha(\lambda)\,x), \tag{24}$$

where $\alpha(\lambda)$ and $R(\lambda)$ are the absorption coefficient and reflectance ($R = (n_2 - n_1)/(n_2 + n_1)$; n_2 = refractive index of the semiconductor; n_1 = refractive index of air) of the semiconductor material, respectively, at a wavelength of λ. The drift component of the photocurrent density ($J_{ps(\mathrm{Opt\ drift})}$ and $J_{ns(\mathrm{Opt\ drift})}$) through the reverse-biased depletion layer is given by

$$J_{ps(\mathrm{Opt\,drift})} = -q\int_{W_{D_n}}^{W_{D_p}} G_L(x)\,dx, \quad \text{in FC structure},$$
$$J_{ns(\mathrm{Opt\,drift})} = -q\int_{W'_{D_p}}^{W'_{D_n}} G_L(x)\,dx, \quad \text{in TM structure}. \tag{25}$$

Due to very high conductivity, electric fields at the p^+- and n^+-layers are zero. Diffusion components of the photocurrent are generated within these undepleted p^+- and n^+-layers. Diffusion components of the photocurrent in both p^+- and n^+-layers separately can be determined by solving the one-dimensional diffusion equation with proper boundary conditions [37]. The electron and hole diffusion components of the photocurrent density ($J_{ps(\mathrm{Opt\ diff})}$ and $J_{ns(\mathrm{Opt\ diff})}$) in both p^+- and n^+-layers are given by

$$J_{ns(\mathrm{Opt\,diff})} = qP_{in}\frac{(1 - R(\lambda))\,\lambda}{Ahc}\left(\frac{\alpha(\lambda)\,L_n}{1 + \alpha(\lambda)\,L_n}\right)\exp\left(-\alpha(\lambda)\,W_{D_p}\right), \quad \text{in FC structure},$$
$$J_{ps(\mathrm{Opt\,diff})} = qP_{in}\frac{(1 - R(\lambda))\,\lambda}{Ahc}\left(\frac{\alpha(\lambda)\,L_p}{1 + \alpha(\lambda)\,L_p}\right)\exp\left(-\alpha(\lambda)\,W'_{D_n}\right) \quad \text{in TM structure}. \tag{26}$$

Total photocurrent density is the combination of drift and diffusion components, that is,

$$J_{ps(\mathrm{Opt})} = J_{ps(\mathrm{Opt\,drift})} + J_{ps(\mathrm{Opt\,diff})}, \quad \text{in FC structure},$$
$$J_{ns(\mathrm{Opt})} = J_{ns(\mathrm{Opt\,drift})} + J_{ns(\mathrm{Opt\,diff})}, \quad \text{in TM structure}. \tag{27}$$

When the light is shined on the n^+-side of the p^+-p-n-n^+ structured RAPD, then the photocurrent density will be hole dominated. For this case, the electron and hole multiplication factors at the n- and p-depletion layer edges are given by

$$M_n\left(x = W_{D_p}\right) = \frac{J_T}{J_{ns(\mathrm{Th})}},$$
$$M'_p\left(x = W_{D_n}\right) = \frac{J_T}{J_{ps(\mathrm{Th})} + J_{ps(\mathrm{Opt})}}. \tag{28}$$

In this case, the value of $M'_p(x = W_{D_n})$ is considerably reduced, while $M_n(x = W_{D_p})$ remains unchanged. Thus, the normalized current density boundary conditions at the depletion layer edges (18a) are modified to

$$P\left(x = W_{D_n}\right) = \left(\frac{2}{M'_p\left(x = W_{D_n}\right)} - 1\right), \quad P\left(x = W_{D_p}\right) = 1 \quad \text{in FC structure}, \tag{29}$$

where $M_n(x = W_{D_p})$ is very large (~10^6) near the breakdown of the device and $M'_p(x = W_{D_n})$ is much smaller than $M_n(x = W_{D_p})$ under similar condition. Equation (29) is used as one of the boundary conditions in the proposed model (in place of (18a)) for simulating the optoelectric properties of the n^+-layer illuminated p^+-p-n-n^+ structured RAPD.

When the light is shined on the p^+-side of the p^+-p-n-n^+ structured RAPD, then the photocurrent density will be

electron dominated. So, the electron and hole multiplication factors at the n- and p-depletion layer edges are given by

$$M_n'\left(x = W_{D_p}'\right) = \frac{J_T}{J_{ns(\mathrm{Th})} + J_{ns(\mathrm{Opt})}},$$
$$M_p\left(x = W_{D_n}'\right) = \frac{J_T}{J_{ps(\mathrm{Th})}}. \quad (30)$$

In this case, the value of $M_n'(x = W_{D_p}')$ is considerably reduced, while $M_p(x = W_{D_n}')$ remains unchanged. Thus, the normalized current density boundary conditions at the depletion layer edges (18b) are modified to

$$P\left(x = W_{D_p}'\right) = \left(1 - \frac{2}{M_n'\left(x = W_{D_p}'\right)}\right), \quad P\left(x = W_{D_n}'\right) = -1, \quad \text{in TM structure,} \quad (31)$$

where $M_p(x = W_{D_n}')$ is very large (~10^6) near the breakdown of the device and $M_n'(x = W_{D_p}')$ is much smaller than $M_p(x = W_{D_n}')$ under similar condition. Equation (31) is used as one of the boundary conditions in the proposed model (in place of (18b)) for simulating the optoelectric properties of the p^+-layer illuminated p^+-p-n-n^+ structured RAPD. Total primary unmultiplied photocurrent (I_{ph}) can be written as

$$I_{ph} = \left(J_{ps(\mathrm{Opt})} + J_{ns(\mathrm{Opt})}\right) A_j. \quad (32)$$

Total multiplied photocurrent (I_M) is given by

$$I_{M'} = \left(M_p' J_{ps(\mathrm{Opt})} + M_n J_{ns(\mathrm{Opt})}\right) A_j, \quad \text{in FC structure,}$$
$$I_{M''} = \left(M_p J_{ps(\mathrm{Opt})} + M_n' J_{ns(\mathrm{Opt})}\right) A_j, \quad \text{in TM structure.} \quad (33)$$

In the avalanche phenomenon of reverse biased p^+-p-n-n^+ structured RAPDs, both electrons and holes participate; a mean value of multiplication factor or optical gain can be expressed as

$$M' = \frac{I_M}{I_{ph}} = \frac{\left(M_p' J_{ps(\mathrm{Opt})} + M_n J_{ns(\mathrm{Opt})}\right)}{\left(J_{ps(\mathrm{Opt})} + J_{ns(\mathrm{Opt})}\right)}, \quad \text{in FC structure,}$$
$$M'' = \frac{I_M}{I_{ph}} = \frac{\left(M_p J_{ps(\mathrm{Opt})} + M_n' J_{ns(\mathrm{Opt})}\right)}{\left(J_{ps(\mathrm{Opt})} + J_{ns(\mathrm{Opt})}\right)}, \quad \text{in TM structure.} \quad (34)$$

where $M_{p/n}'$ and $M_{p/n}''$ are the overall multiplication factors which are obtained by integrating the position dependent multiplication factor ($M_{p/n}'(x)$ and $M_{p/n}''(x)$) over the entire depletion layer width. The responsivity (R' or $R''AW^{-1}$) of an APD is defined as the output photocurrent per unit incident optical power which can be written as

$$R' = \frac{I_{M'}}{P_{in}} = M' \frac{I_{ph}}{P_{in}} = M' \cdot R_{ug}, \quad \text{in FC structure,}$$
$$R'' = \frac{I_{M''}}{P_{in}} = M'' \frac{I_{ph}}{P_{in}} = M'' \cdot R_{ug}, \quad \text{in TM structure,} \quad (35)$$

where R_{ug} is the unity gain responsivity of the device.

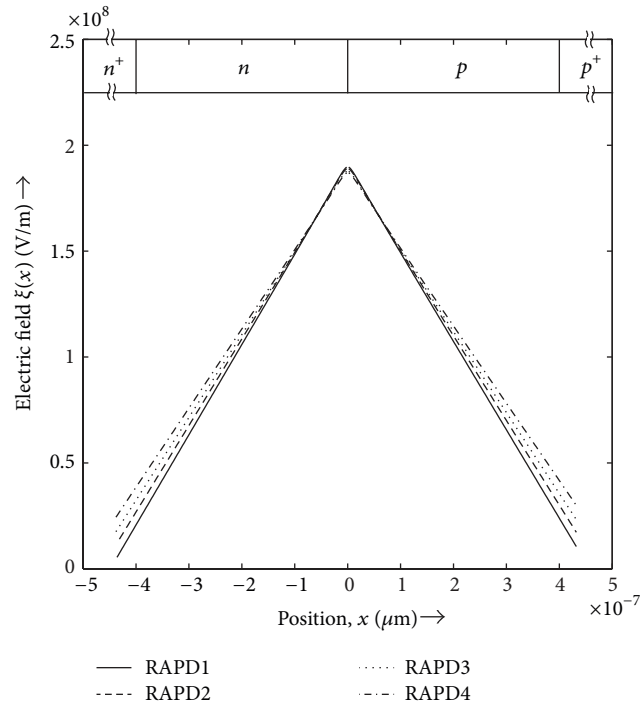

Figure 4: Electric field profiles of unilluminated p^+-p-n-n^+ Wz-GaN RAPDs near breakdown.

5. Results and Discussion

Simulation is carried out to study the electrical and optoelectrical characteristics of the designed p^+-p-n-n^+ structured Wz-GaN RAPDs (Table 1). The effect of optical illumination on the electric field profile of the device is investigated for two different optical illumination configurations. Simulated electric field profiles are shown in Figure 4 near breakdown voltages. Breakdown voltages (V_B) of RAPD1, RAPD2, RAPD3, and RAPD4 are calculated by integrating the electric field profiles within the entire depletion regions of the corresponding devices (i.e., $V_B = \int_W \xi(x)dx$, where $W = W_n + W_p$). Breakdown voltages of RAPD1, RAPD2, RAPD3, and RAPD4 are obtained as 85.54, 89.25, 91.46, and 94.47 V, respectively. Breakdown voltage increases as the doping levels of the active layers decrease. Spatial variations of impact ionization rates for electrons (α_n) and holes (α_p) in p^+-p-n-n^+ structured Wz-GaN RAPDs are shown in Figure 5. It is interesting to observe that the ionization rates for holes (α_p) are higher compared to the ionization rate of electrons (α_n) at

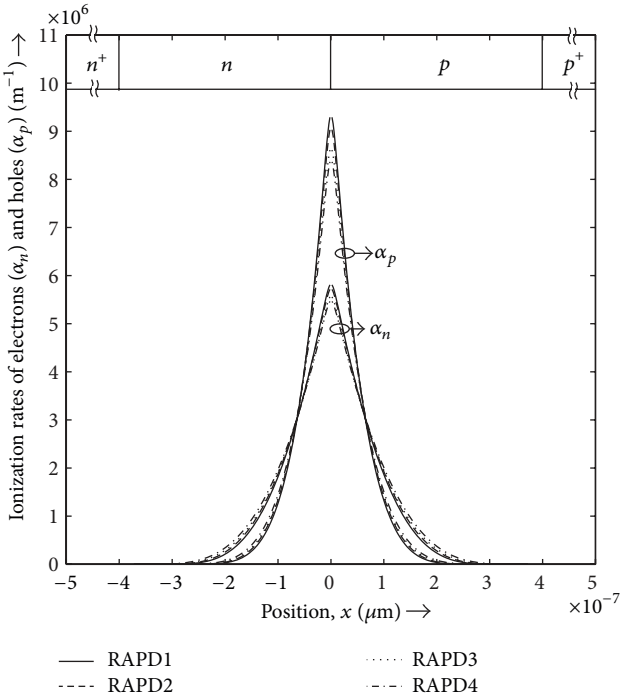

FIGURE 5: Spatial distributions of electron and hole ionization rates in unilluminated p^+-p-n-n^+ Wz-GaN RAPDs near breakdown.

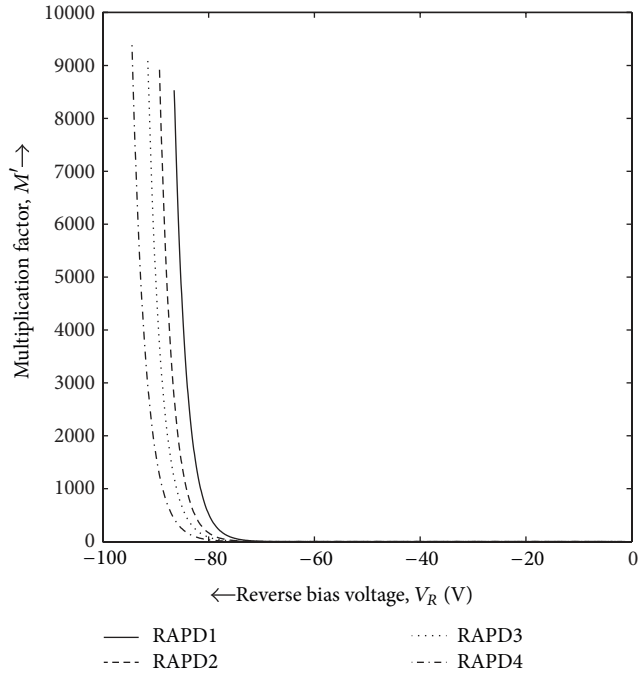

FIGURE 6: Variations of multiplication factors with reverse bias voltage in p^+-p-n-n^+ Wz-GaN RAPDs due to optical illumination (λ = 365 nm) on the n^+-layer (FC).

each space points within the active region of the device. Also, both α_p and α_n are higher at each space points within its low field regions in RAPDs with lower doping levels because at low field regions, electric fields at each space point, higher for lower doping level RAPDs. But the peak electric field at the metallurgical junction increases with the increase of doping concentration (Figure 4), and thus, at the junction both, α_p and α_n are higher in RAPDs having higher doping levels (Figure 5).

Multiplication factors (M', M'') of the RAPDs under consideration are plotted against reverse bias voltage (V_R) for both types of optical illumination configurations (i.e., FC and TM) for 365 nm wavelength in Figures 6 and 7. It is observed that peak multiplication factor is higher for hole dominated photocurrent (highest 9.4144×10^3), that is, when the UV light is shined on the n^+-layer of the device (FC structure) as compared to that of the electron dominated photocurrent (highest 7.8800×10^3), that is, when the UV light is shined on the p^+-layer of the device (TM structure). It is occurred because the ionization rate of holes (α_p) is higher than that of electrons (α_n) in Wz-GaN [22]; thus, the hole dominated photocurrent ($I_{M'}$) must have greater value in FC structure as compared to electron dominated photocurrent ($I_{M''}$) in TM structure, since greater impact ionization occurs in FC structure. That is why Wz-GaN-based APDs are more sensitive to hole dominated photocurrent causing greater multiplication gain in FC structure as compared to TM structure. This effect is similar as InP- and GaAs-based avalanche transit time (ATT) devices [38–40] where $\alpha_p > \alpha_n$, but opposite of Si-based ATT devices [40–48] where $\alpha_n > \alpha_p$. Also, multiplication factor is higher for lower doping level RAPDs due to their expected wider avalanche zones or multiplication regions.

Figure 8 shows the variations of electron dominated photocurrent ($I_{M''}$: TM structure), hole dominated photocurrent ($I_{M'}$: FC structure), and total dark current (I_T: without illumination) with reverse bias voltage in RAPD4. The simulated photocurrents that are shown in Figure 8 are for optical illumination of wavelength λ = 365 nm. Also, the dark current components due to band-to-band tunneling (I_{BBT}) and trap-assisted tunneling (I_{TAT}: for three different trap centers E_t = 0.20, 0.40, and 0.60 eV) are also shown in Figure 8. It can be observed that both I_{BBT} and I_{TAT} are increasing with the increase of reverse bias (V_R), that is, with the increase of electric field across the depletion region. It is also noteworthy that the magnitudes of I_{BBT} and I_{TAT} are much lower as compared to the total current (I_T) through the device under unilluminated condition the breakdown. Thus, the avalanche multiplication phenomenon is clearly dominant over the both types of tunneling phenomena (band-to-band and trap-assisted). It can be observed from Figure 8 that at low reverse bias when the amount of impact ionization is low (causing very low multiplication gain (M', M'')) in both the electron and hole dominated photocurrents which are much higher (~10^{-9} to ~10^{-8} A for $|V_R|$ = 0 to 40 V) as compared to the dark current (10^{-13} to 10^{-11} A for $|V_R|$ = 0 to 40 V). But the dark current grows with much faster rate as compared to the photocurrents as the reverse bias increases further and near the breakdown (when the multiplication gain (M', M'') is very high (~10^4)) dark current and photocurrents are almost comparable. Thus,

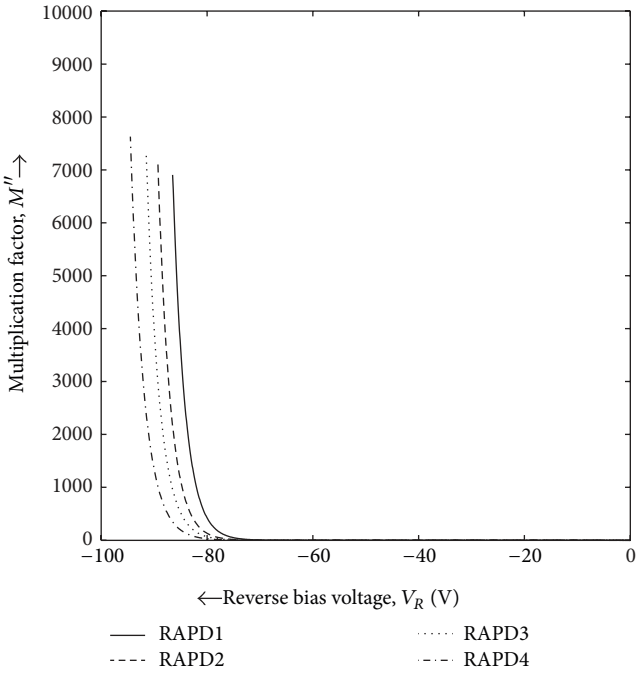

Figure 7: Variations of multiplication factors with reverse bias voltage in p^+-p-n-n^+ Wz-GaN RAPDs due to optical illumination (λ = 365 nm) on the p^+-layer (TM).

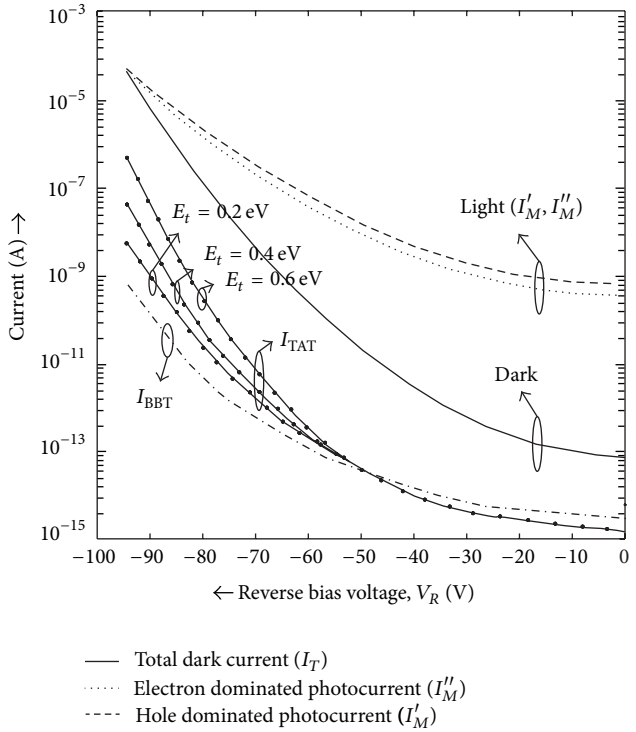

Figure 8: Variations electron and hole dominated photocurrents (for optical illumination of wavelength λ = 365 nm), total dark current, band-to-band tunneling current and trap-assisted tunneling current (for different trap centers) with reverse bias voltage in RAPD4.

the APDs must be biased well below the breakdown voltage so that amount of dark current remains much smaller as compared to the photocurrent component. But the reverse bias should not be very low (<40 V) because, at very low reverse bias, multiplication gain (M', M'') is very low which is not sufficient to detect very weak optical signals. In the case of RAPDs under consideration, applied reverse bias must be 40 to 85 V. It is also noteworthy from Figure 8 that the hole dominated photocurrent ($I_{M'}$) is higher as compared to electron dominated photocurrent ($I_{M''}$); which reconfirms the greater sensitivity of Wz-GaN RADPs in hole dominated photocurrent.

Unity gain responsivity curves of p^+-p-n-n^+ structured Wz-GaN RAPDs are shown in Figures 9 and 10 for both type of optical illumination configurations (FC and TM). Unity gain responsivities are calculated for the wavelength 300–450 nm, and it is observed that the peak responsivity is obtained at 365 nm for both FC and TM structures. Again, peak responsivities are higher (555.78 mA W^{-1} at 365 nm) for hole dominated photocurrent, that is, in FC structure as compared to electron dominated photocurrent (480.56 mA W^{-1} at 365 nm), that is, in TM structure. It is also interesting to observe that due to wider avalanche widths (i.e., higher impact ionization), lower doping level RAPDs provide higher responsivity due to same amount of incident optical power at same reverse bias. It can be noticed from Figures 9 and 10 that in both the optical illumination configurations (FC and TM) the device shows responsivity peaks at 365 nm wavelength which is also observed in the earlier experimental report on GaN APDs [19].

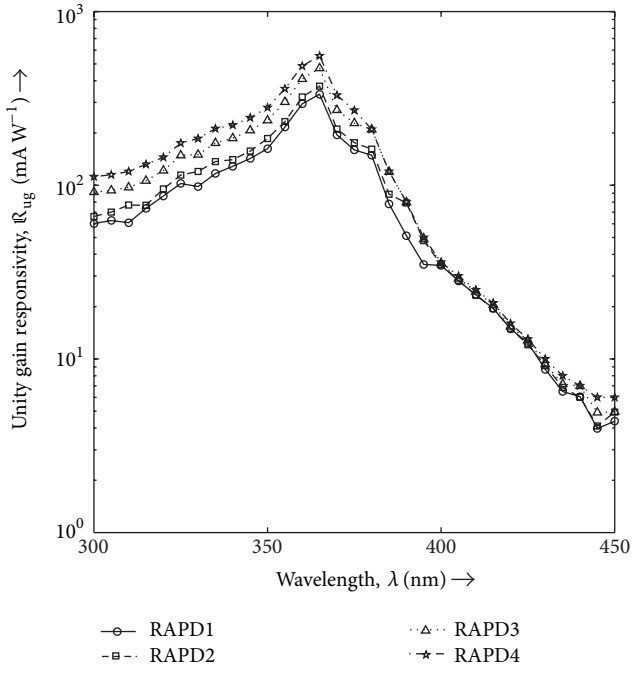

Figure 9: Variations of unity gain spectral responsivities with wavelength in p^+-p-n-n^+ Wz-GaN RAPDs due to optical illuminated on the n^+-layer (FC) for applied reverse bias of 85 V.

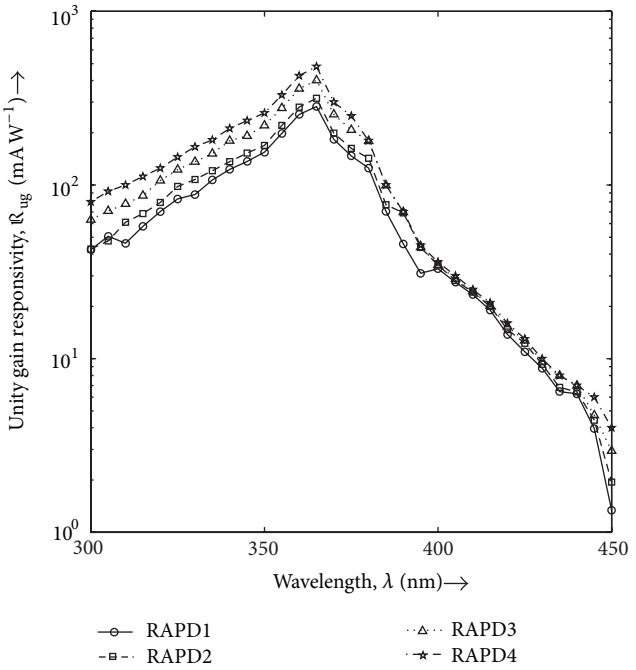

FIGURE 10: Variations of unity gain spectral responsivities with wavelength in p^+-p-n-n^+ Wz-GaN RAPDs due to optical illuminated on the p^+-layer (TM) for applied reverse bias of 85 V.

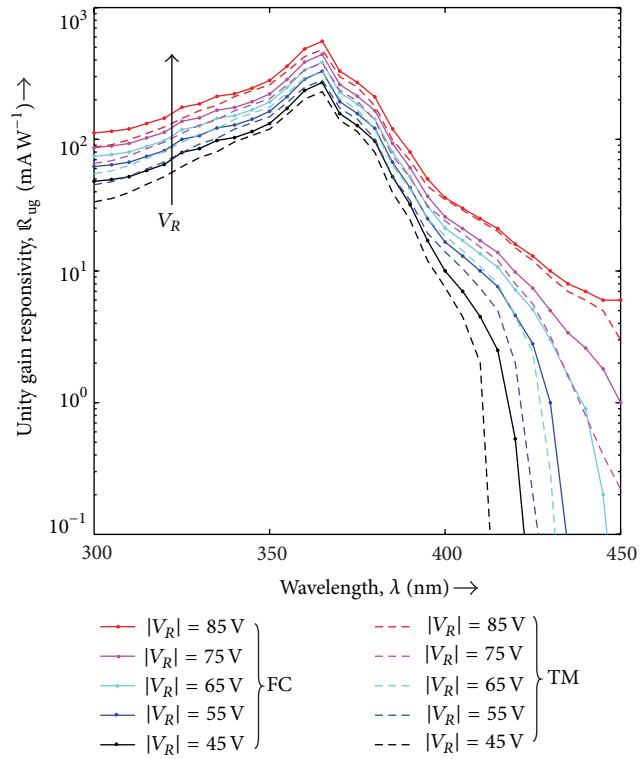

FIGURE 11: Variations of unity gain spectral responsivities with wavelength in RAPD4 for different reverse bias under both FC and TM configurations.

Spectral response of RAPD4 is shown in Figure 11 as a function of reverse bias voltage under both optical illumination configurations. It can be observed from Figure 11 that in both FC and TM structures the peak unity gain responsivity (at 365 nm) increases as the reverse bias voltage increases. Peak unity gain responsivity increases from 269.92 to 555.78 mA W^{-1} as the reverse bias voltage increases from 45 to 85 V in FC structure, whereas the same increases from 229.87 to 480.56 mA W^{-1} for the same increment of reverse bias. Also, it is noteworthy that the unity gain responsivity at each wavelength is higher in FC structure (i.e., for hole dominated photocurrent) as compared to that in TM structure (i.e., for electron dominated photocurrent) for a particular reverse bias voltage.

6. Validation of the Simulation Results

Vashaei et al. [19] fabricated GaN avalanche p-i-n photodiodes grown on m-plane freestanding GaN substrate and experimentally studied spectral response of the device. The photocurrent was extracted by measuring the I-V characteristics under white light illumination using a Xenon lamp coupled onto the top of the device (p-layer) through an UV fiber-optic cable. The spectral response of the devices was measured within the wavelength range of 300 to 450 nm. They obtained peak unity gain responsivity of the device more than 523.0 mA W^{-1} at 364 nm with multiplication factor of about 8,000 at an applied reverse bias of 75 V. The simulation results presented in this paper show that 555.78 mA W^{-1} of peak unity gain responsivity at 365 nm wavelength may be achieved with a multiplication factor of 9.4144×10^3 in p^+-p-n-n^+ structured Wz-GaN RAPD when the UV light is illuminated on the n^+-layer of the device (i.e., FC structure) in which the photocurrent is hole dominated, whereas those are 480.56 mA W^{-1} and 7.8800×10^3, respectively, when UV light of same wavelength is illuminated on the p^+-layer of the device, that is, due to electron dominated photocurrent (i.e., in TM structure) (applied reverse bias V_R = 85 V for both of these FC and TM structures). Thus, the simulation results are in close agreement with the experimentally obtained results of Vashaei et al. [19]. Slight deviation in the simulation results from the experimental results may be due to the difference in structure of the devices and different electrical bias conditions.

7. Conclusions

The effect of electron versus hole photocurrent on the optoelectric properties of p^+-p-n-n^+ structured Wz-GaN RAPDs is investigated in this paper within visible-blind UV range (300–450 nm). Results show that peak unity gain responsivity of 555.78 mA W^{-1} at 365 nm can be achieved with a multiplication factor of 9.4144×10^3 when light is illuminated on the n^+-layer of the device, that is, when the photocurrent is hole dominated (FC structure), while those are 480.56 mA W^{-1} and 7.8800×10^3, respectively, when light of same wavelength

is illuminated on the p^+-layer of the device, that is, due to electron dominated photocurrent (i.e., in TM structure) (applied reverse bias $V_R = 85$ V for both of these FC and TM structures). Due to higher hole ionization rate compared to electron ionization rate ($\alpha_p > \alpha_n$) in Wz-GaN, the p^+-p-n-n^+ structured Wz-GaN RAPDs are more sensitive to hole dominated photocurrent as compared to electron dominated photocurrent. So, it can be concluded that UV light has to be illuminated on n^+-layer of the device instead of p^+-layer to get better optoelectrical performance of Wz-GaN RAPDs. Results are extremely encouraging to fabricate p^+-p-n-n^+ structured Wz-GaN RAPDs for high performance visible-blind UV applications such as bioaerosol detection, UV imaging, harsh environment gamma sensing, long-range flame detection in the solar-blind window.

References

[1] G. Pietri, "Progress in photomultiplier tubes for scintillation counting and nuclear physics," *IRE Transactions on Nuclear Science*, vol. 9, no. 3, pp. 62–72, 1962.

[2] G. A. Shaw, A. M. Siegel, J. Model et al., "Deep UV photon-counting detectors and applications," in *Advanced Photon Counting Techniques III*, vol. 7320 of *Proceedings of SPIE*, pp. 1–15, April 2009.

[3] I. Węgrzecka, M. Węgrzecki, M. Grynglas et al., "Design and properties of silicon avalanche photodiodes," *Opto-Electronics Review*, vol. 12, no. 1, pp. 95–104, 2004.

[4] T. Kaneda, "Chapter 3 silicon and germanium avalanche photodiodes," *Semiconductors and Semimetals*, vol. 22, pp. 247–328, 1985.

[5] R. D. Dupuis, J. H. Ryou, D. Yoo et al., "High-performance GaN and $Al_xGa_{1-x}N$ ultraviolet avalanche photodiodes grown by MOCVD on bulk III-N substrates," in *Electro-Optical Remote Sensing, Detection, and Photonic Technologies and Their Applications*, vol. 6739 of *Proceedings of SPIE*, September 2007.

[6] X. Bai, H. D. Liu, D. C. Mcintosh, and J. C. Campbell, "High-detectivity and high-single-photon-detectionefficiency 4H-SiC avalanche photodiodes," *IEEE Journal of Quantum Electronics*, vol. 45, no. 3, pp. 300–303, 2009.

[7] E. J. Tarsa, P. Kozodoy, J. Ibbetson, B. P. Keller, G. Parish, and U. Mishra, "Solar-blind AlGaN-based inverted heterostructure photodiodes," *Applied Physics Letters*, vol. 77, no. 3, pp. 316–318, 2000.

[8] C. Bayaram, J. L. Pau, R. McClintock, and M. Razeghi, "Performance enhancement of GaN ultraviolet avalanche photodiodes with p-type δ-doping," *Applied Physics Letters*, vol. 92, no. 24, Article ID 241103, 3 pages, 2008.

[9] P. Schreiber et al., "A perspective of GaN/AlGaN detector development for UV missile warning applications," Proceedings of the 6th International Workshop on Wide Bandgap III-Nitrides, Richmond, Va, USA, March 2000.

[10] J. D. Brown, Y. Zhonghai, J. Mattews et al., "Visible-blind UV digital camera based on a 32 × 32 array of GaN/AlGaN p-i-n photodiodes," *MRS Internet Journal of Nitride Semiconductor Research*, vol. 4, no. 9, pp. 1–5, 1999.

[11] G. Parish, S. Keller, P. Kozodoy et al., "High-performance (Al,Ga) N-based solar-blind ultraviolet p-i-n detectors on laterally epitaxially overgrown GaN," *Applied Physics Letters*, vol. 75, no. 2, pp. 247–2249, 1999.

[12] D. Walker, V. Kumar, K. Mi et al., "Solar-blind AlGaN photodiodes with very low cutoff wavelength," *Applied Physics Letters*, vol. 76, no. 4, pp. 403–405, 2000.

[13] K. A. McIntosh, R. J. Molnar, L. J. Mahoney et al., "GaN avalanche photodiodes grown by hydride vapor-phase epitaxy," *Applied Physics Letters*, vol. 75, no. 22, pp. 3485–3487, 1999.

[14] J. C. Carrano, D. J. H. Lambert, C. J. Eiting et al., "GaN avalanche photodiodes," *Applied Physics Letters*, vol. 76, no. 7, pp. 924–926, 2000.

[15] K. A. McIntosh, R. J. Molnar, L. J. Mahoney, K. M. Molvar, N. Efremow, and S. Verghese, "Ultraviolet photon counting with GaN avalanche photodiodes," *Applied Physics Letters*, vol. 76, no. 26, pp. 3938–3940, 2000.

[16] B. Monemar, O. Lagerstedt, and H. P. Gislason, "Properties of Zn-doped VPE-grown GaN. I. Luminescence data in relation to doping conditions," *Journal of Applied Physics*, vol. 51, no. 1, pp. 625–639, 1980.

[17] S. Verghese, K. A. McIntosh, R. J. Molnar et al., "GaN avalanche photodiodes operating in linear-gain mode and Geiger mode," *IEEE Transactions on Electron Devices*, vol. 48, no. 3, pp. 502–511, 2001.

[18] V. A. Joshkin, C. A. Parker, S. M. Bedair et al., "Effect of growth temperature on point defect density of unintentionally doped GaN grown by metalorganic chemical vapor deposition and hydride vapor phase epitaxy," *Journal of Applied Physics*, vol. 86, no. 1, pp. 281–288, 1999.

[19] Z. Vashaei, E. Cicek, C. Bayram, R. McClintock, and M. Razeghi, "GaN avalanche photodiodes grown on m-plane freestanding GaN substrate," *Applied Physics Letters*, vol. 96, no. 20, Article ID 201908, 2010.

[20] A. Acharyya and J. P. Banerjee, "Design and simulation of silicon carbide poly-type double-drift region avalanche photodiodes for UV sensing," *Journal of Optoelectronics and Advanced Materials*, vol. 14, no. 7-8, pp. 630–639, 2012.

[21] M. Ghosh, M. Mondal, and A. Acharyya, "4H-Sic avalanche photodiodes as uv sensors: a brief review," *Journal of Electron Devices*, vol. 15, pp. 1291–1295, 2012.

[22] K. Kunihiro, K. Kasahara, Y. Takahashi, and Y. Ohno, "Experimental evaluation of impact ionization coefficients in GaN," *IEEE Electron Device Letters*, vol. 20, no. 12, pp. 608–610, 1999.

[23] B. Kramer and A. Micrea, "Determination of saturated electron velocity in GaAs," *Applied Physics Letters*, vol. 26, pp. 623–6624, 1975.

[24] S. Chen and G. Wang, "High-field properties of carrier transport in bulk wurtzite GaN: a Monte Carlo perspective," *Journal of Applied Physics*, vol. 103, no. 2, Article ID 023703, 2008.

[25] Electronic Archive, "New Semiconductor Materials, Characteristics and Properties," 2013, http://www.ioffe.ru/SVA/NSM/Semicond.

[26] G. Yu, G. Wang, H. Ishikawa et al., "Optical properties of wurtzite structure GaN on sapphire around fundamental absorption edge (0.78–4.77 eV) by spectroscopic ellipsometry and the optical transmission method," *Applied Physics Letters*, vol. 70, no. 24, pp. 3209–3211, 1997.

[27] J. F. Muth, J. H. Lee, I. K. Shmagin et al., "Absorption coefficient, energy gap, exciton binding energy, and recombination lifetime of GaN obtained from transmission measurements," *Applied Physics Letters*, vol. 71, no. 18, pp. 2572–2574, 1997.

[28] J. M. senior, *Optical Fiber Communications: Principles and Practice*, Pearson Education, 2nd edition, 2007.

[29] G. Ariyawansa, M. B. M. Rinzan, M. Strassburg et al., "GaN/AlGaN heterojunction infrared detector responding in 8-14 and 20-70 μm ranges," *Applied Physics Letters*, vol. 89, no. 14, Article ID 141122, 2006.

[30] M. E. Elta, "The effect of mixed tunneling and avalanche breakdown on microwave transit-time diodes," Tech. Rep. 142, Electron Physics Laboratory, University of Michigan, Ann Arbor, Mich, USA, 1978.

[31] M. E. Elta and G. I. Haddad, "Mixed tunneling and avalanche mechanism in p-n junctions and their effects on microwave transit time devices," *IEEE Transactions on Electron Devices*, vol. 25, no. 6, pp. 694–702, 1978.

[32] E. O. Kane, "Theory of tunneling," *Journal of Applied Physics*, vol. 32, no. 1, pp. 83–91, 1961.

[33] G. N. Dash and S. P. Pati, "Generalized simulation method for MITATT-mode operation and studies on the influence of tunnel current on IMPATT properties," *Semiconductor Science and Technology*, vol. 7, no. 2, pp. 222–230, 1992.

[34] A. Acharyya, M. Mukherjee, and J. P. Banerjee, "Influence of tunnel current on DC and dynamic properties of silicon based terahertz IMPATT source," *Terahertz Science and Technology*, vol. 4, pp. 26–241, 2011.

[35] V. Gopal, S. K. Singh, and R. M. Mehra, "Analysis of dark current contributions in mercury cadmium telluride junction diodes," *Infrared Physics and Technology*, vol. 43, no. 6, pp. 317–326, 2002.

[36] R. J. McIntyre, "Multiplication noise in uniform avalanche diodes," *IEEE Transactions on Electron Devices*, vol. 13, pp. 164–1168, 1966.

[37] S. M. Sze and K. K. Ng, *Physics of Semiconductor Devices*, John Wiley & Sons, Madras, India, 3rd edition, 2010.

[38] J. P. Banerjee, R. Mukherjee, J. Mukhopadhyay, and P. N. Mallik, "Studies on avalanche phase delay and the admittance of an optically illuminated indium phosphide avalanche transit time diode at millimeter wave window frequencies," *Physica Status Solidi A*, vol. 153, no. 2, pp. 567–579, 1996.

[39] J. P. Banerjee and R. Mukherjee, "Effect of electron- and hole-dominant photocurrent on the millimetre wave properties of an indium phosphide IMPATT diode at a 94 GHz window under optical illumination," *Semiconductor Science and Technology*, vol. 9, no. 9, pp. 1690–1695, 1994.

[40] H. W. Yen, M. K. Barnoski, R. G. Hunsperger, and R. T. Melville, "Switching of GaAs IMPATT diode oscillator by optical illumination," *Applied Physics Letters*, vol. 31, no. 2, pp. 120–122, 1977.

[41] A. Acharyya, S. Banerjee, and J. P. Banerjee, "Optical control of millimeter-wave double-drift region silicon IMPATT device," *Radioengineering*, vol. 21, pp. 1208–1217, 2012.

[42] A. Acharyya and J. P. Banerjee, "Analysis of photo-irradiated double-drift region silicon impact avalanche transit time devices in the millimeter-wave and terahertz regime," *Terahertz Science and Technology*, vol. 5, no. 2, pp. 97–113, 2012.

[43] A. Acharyya and J. P. Banerjee, "A comparative study on the effect of optical illumination on $Si_{1-x}Ge_x$ and Si based DDR IMPATT diodes at W-band," *Iranian Journal of Electronics and Electrical Engineering*, vol. 7, no. 3, pp. 179–189, 2011.

[44] H. P. Vyas, R. J. Gutmann, and J. M. Borrego, "The effect of hole versus electron photocurrent on microwave-optical interactions in IMPATT oscillators," *IEEE Trans Electron Devices*, vol. 26, no. 3, pp. 232–234, 1979.

[45] A. J. Seeds and A. A. A. De Salles, "Optical control of microwave semiconductor devices," *IEEE Transactions on Microwave Theory and Techniques*, vol. 38, no. 5, pp. 577–585, 1990.

[46] J. R. Forrest and A. J. Seeds, "Optical injection locking of impatt oscillators," *Electronics Letters*, vol. 14, no. 19, pp. 626–627, 1978.

[47] A. Schweighart, H. P. Vyas, J. M. Borrego, and R. J. Gutmann, "Avalanche diode structures suitable for microwave-optical interactions," *Solid State Electronics*, vol. 21, no. 9, pp. 1119–1121, 1978.

[48] H. P. Vyas, R. J. Gutmann, and J. M. Borrego, "Leakage current enhancement in IMPATT oscillator by photo-excitation," *Electronics Letters*, vol. 13, no. 7, pp. 189–190, 1977.